ACS APPLIED MATERIALS & INTERFACES

www.acsami.org Research Article

Understanding the Kinetics of CO_2 Hydrate Formation in Dry Water for Carbon Capture and Storage: X-ray Diffraction and In Situ Raman Studies

Gaurav Vishwakarma,[‖] Vikas Dhamu,[‖] M. Fahed Qureshi, Gaurav Bhattacharjee, Thalappil Pradeep,* and Praveen Linga*

Cite This: https://doi.org/10.1021/acsami.4c17727 Read Online

ACCESS | Metrics & More | Article Recommendations | Supporting Information

ABSTRACT: Hydrate-based carbon capture and storage (HBCS) is a sustainable and promising approach to combating global warming by utilizing water, which is a ubiquitous resource. Here, we report a comprehensive study of CO_2 hydrate formation in dry water (DW), a water-in-air dispersion confined in silica particles, for improving the kinetics of hydrate growth. Utilizing a combination of a home-built high-pressure reactor, in situ Raman spectroscopy, and powder X-ray diffraction (PXRD), we elucidate the crystal structure, growth dynamics, and morphology of CO_2 hydrates formed in DW, with and without the kinetic hydrate promoter, L-tryptophan. Our analysis reveals that CO_2 forms structure I (sI) hydrate in DW, with hydrate growth occurring both on and beneath the silica shell. This results in a substantial increase in CO_2 uptake—approximately 2.8 times higher than that observed in pure water (~134 v/v compared to ~48 v/v). Moreover, incorporation of L-tryptophan in DW formation markedly accelerates the DW-CO_2 hydrate formation process, reducing both the induction time and the time required to achieve 90% gas uptake at 274.65 K. These findings offer crucial insights into the formation of CO_2 hydrate in DW, highlighting its potential to improve the efficiency and scalability of HBCS technologies.

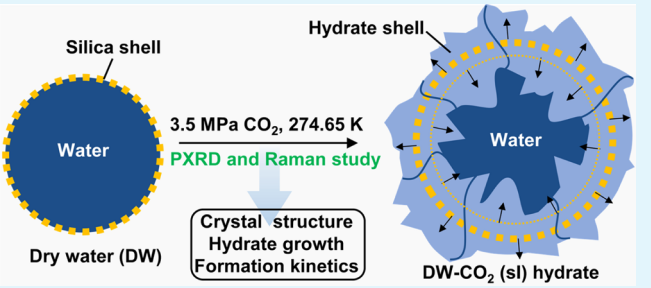

KEYWORDS: *CO_2 hydrates, dry water, carbon capture and storage, Raman spectroscopy, X-ray diffraction*

1. INTRODUCTION

Excess CO_2 emissions in the atmosphere are considered a primary source of global warming. A 50% reduction in CO_2 emissions by 2030 is required to obtain a zero-carbon economy by 2050.[1] To restrict global temperature from rising more than 2 °C and limit CO_2 emissions to 1100 gigatons (2011−2050), it is essential to use carbon capture and storage (CCS) techniques, along with other renewable technologies.[2−4] Using gas hydrates for CCS is one of the potential techniques, as they offer a high theoretical storage capacity of about 180 v/v (volume of gas at STP/volume of hydrate).[5,6] Gas hydrates are crystalline, nonstoichiometric host−guest compounds that form when guest molecules are encapsulated within hydrogen-bonded water cages under high-pressure and low-temperature conditions.[7] Moreover, gas hydrates have been widely studied across diverse experimental conditions[8−14] and through computational approaches.[15−17] Gas hydrates naturally exist in permafrost zones[18,19] and are speculated to exist in interstellar medium and within the solar system.[20−22] These compounds are often classified into three distinct structures: structure I (sI, cubic, two small 5^{12}, and six large $5^{12}6^2$ cages per unit cell), structure II (sII, cubic, 16 small 5^{12}, and eight large $5^{12}6^4$ cages per unit cell), and structure H (sH, hexagonal).[23,24] Analogous to natural gas hydrates, researchers are investigating the possibility of storing industrial CO_2 emissions in the form of CO_2 hydrates.[25−27] However, this faces several challenges, including the sluggish rate of CO_2 hydrate formation and low water-to-hydrate conversion.[28−31]

To enhance clathrate hydrate formation kinetics, increasing the contact between liquid (water) and gas (guest) is the key.[7] Methods to achieve this include the use of high pressures, vigorous mixing, ice particles, surfactants, amino acids, dry water (DW), etc.[32] Among these, DW, a powder made from blending water, air, and hydrophobic nanosilica particles, is noted for its high gas storage capacity and faster formation rates.[32,33] DW consists of minuscule water droplets, called water pools, enclosed by a hydrophobic nanosilica layer that prevents the droplets from merging.[34] The enhanced storage capacity in DW-gas hydrates can be attributed to its higher

Received: October 15, 2024
Revised: December 1, 2024
Accepted: December 31, 2024

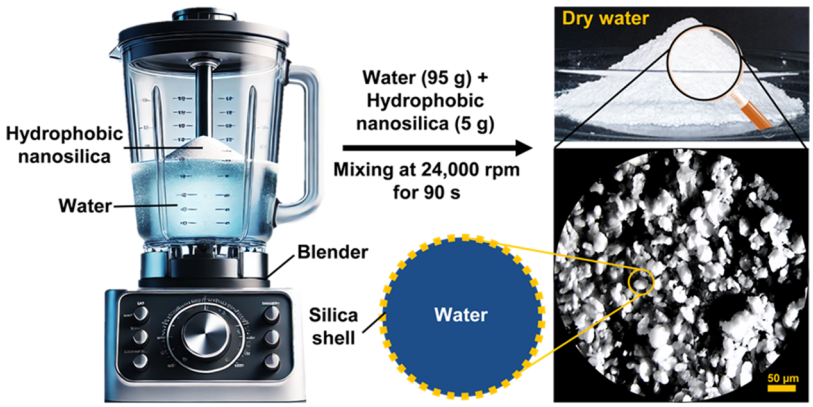

Figure 1. DW Preparation: 5 g of hydrophobic nanosilica was blended with 95 g of water at 24,000 rpm for 90 s to produce DW powder. The figure shows an illustration of the blender, a photograph of the prepared DW, and an optical micrograph of DW (scale bar = 50 μm). Inset provides a schematic representation of DW, where water is depicted in blue and silica particles in yellow. The micrograph was captured using an Olympus SZX16 microscope.

surface-to-volume ratio than bulk water.[32,35] Recent studies show that DW significantly accelerated the hydrate formation kinetics of several gases (e.g., CH_4, CO_2, Kr, C_2H_6, etc.) and should be further explored as a potential medium for synthesizing bulk CH_4 and CO_2 hydrates for storage and transportation applications.[32,33,36−40] Wang et al., in one of the initial reports, found that DW-CH_4 hydrate can store about ∼175 v/v of CH_4 at 273.2 K.[32] Carter et al. found that DW can speed up the formation of CO_2 and Kr hydrates.[33] They observed that CO_2 could be stored up to ∼150 v/v in DW at 273.2 K, while the theoretical maximum storage capacity of sI hydrates is ∼180 v/v (STP). The lower CO_2 storage capacity in DW-gas hydrates, according to Carter et al., might be due to the incomplete filling of the sI hydrate cages or the cocrystallization of both sII and sI hydrates. Thus, although several studies have examined gas hydrate formation and growth dynamics in DW, critical aspects of DW and DW-CO_2 hydrates are yet to be fully understood.

Wang et al. identified the potential of using second guest molecules (thermodynamic promoters) to form DW-gas hydrates at pressures much lower than their typical formation pressures.[32] However, attempts to achieve this using thermodynamic promoters such as tetrahydrofuran and tetrabutylammonium bromide were met with limited success, as these compounds disrupted the integrity of DW. In contrast, recent research highlights the potential of using amino acids as kinetic hydrate promoters.[41,42] For instance, Khandelwal et al. showed that L-tryptophan (L-trp) significantly enhances both the formation rate and CO_2 uptake in hydrates, achieving up to a 3-fold increase compared to systems without the promoter. These findings point to the importance of exploring the combined use of eco-friendly amino acids like L-trp with DW, to further enhance CO_2 uptake kinetics above the freezing point.[43,44]

Despite the volume of research on DW-CO_2 hydrates, several fundamental aspects remain unclear, such as the crystal structure, hydrate growth dynamics, combined effect of kinetic hydrate promoters, morphology, and the stability of DW when additives are introduced.[45−48] In other words, comprehensive studies on CO_2 uptake kinetics in DW-gas hydrates are still limited, highlighting the need for further macro- and microscale study to evaluate DW's reusability and commercial potential. The present work examines the CO_2 hydrate formation kinetics in DW with L-trp (0−1000 ppm) at 3.5 MPa and 274.65 K. We found that DW prepared using 500 and 1000 ppm L-trp solution was stable over a few months. The formation kinetics and morphology at the macroscale were investigated using a high-pressure reactor. The crystal structure and hydrate growth dynamics were analyzed at the microscale with powder X-ray diffraction (PXRD) and in situ Raman spectroscopy.

2. EXPERIMENTAL SECTION

2.1. Materials. Hydrophobic nanosilica particles (HDK grade H18, 5−30 nm) and L-tryptophan (L-trp, >99% purity) were supplied by Wacker Chemie and Sigma-Aldrich, respectively. CO_2 gas (>purity 99.9%) was obtained from Air Liquide Singapore Pvt. Ltd. The deionized water was collected from the in-house Merck Millipore Direct-Q 3 UV system, which was used for all experimental trials and for preparing DW.

2.2. Preparation of DW. The deionized water (95 g) was poured into a blender (Vitamix, glass jug blender, 2 L), and 5 g of nanosilica particles were added to it. Mixing was carried out at the highest speed setting (average speed of ∼24,000 rpm) for 90 s, divided into three 30 s bursts. The air/water/silica volume ratio was constant for each DW preparation. The material was produced as a free-flowing, dry, white powder that could be easily transferred between vessels without leaving a residue, indicating the formation of water droplets encapsulated by a silica shell. For visual confirmation, Figure S1 presents a photograph illustrating the transfer of DW from a blender jar to a storage bottle. DW containing L-trp was prepared in the same way using solutions of appropriate concentrations. The DW prepared with a solution containing L-trp was stable over a few months. It should be noted that thermodynamic promoters like tetrahydrofuran and tetrabutylammonium bromide were reported to destabilize the DW.[32] A schematic of the DW preparation is shown in Figure 1.

2.3. Equipment. *2.3.1. High-Pressure Reactor.* A high-pressure reactor (made of SS316) with an internal volume of about 150 mL was used for all macro-kinetics experiments (a schematic diagram of the setup is shown in the Supporting Information, Figure S2). Two acrylic viewing windows, each with a diameter of 3 cm, were installed in the reactor's front and back to monitor the morphology of CO_2 hydrate formation in DW and pure water.[49] To regulate the reactor's temperature, coolant from an external chiller bath was circulated in the cooling jacket of the reactor vessel. Throughout the experiments, the temperature within the system was continuously monitored by using a thermocouple placed at the gas−liquid/DW interface. The pressure inside the crystallizer chamber was monitored with a pressure transducer (PT) with an uncertainty of ±0.1% in the pressure range of 0−3.5 MPa. A data acquisition (DAQ) device linked to the thermocouple and the pressure sensors was used to record the

https://doi.org/10.1021/acsami.4c17727
ACS Appl. Mater. Interfaces XXXX, XXX, XXX−XXX

temperature and pressure data at regular intervals of 10 s. The HD camera was installed at the front window to closely monitor the CO_2 hydrate formation morphology in water/DW.

2.3.2. In Situ Raman Spectroscopy. The in situ Raman spectroscopy analysis was performed using a dispersive laser Raman spectrometer (Model: SRaman-532). The jacketed high-pressure reactor is constructed of stainless steel with an internal volume of about 230 mL (a schematic diagram of the setup is shown in Figure S3). The Raman probe inside the reactor vessel has two optical fibers that transmit the laser to the reactor and the resulting signals back to the spectrometer. Raman experiments were performed with an Nd:Yag laser source (wavelength = 532 nm) with a laser power of ∼42 mW. The acquired spectra span from 150 to 4490 cm^{-1}, with a resolution of 2.8 cm^{-1}/pixel at 2200 cm^{-1}. The procedure for hydrate formation in the in situ Raman analysis was identical to that in macroscale kinetic experiments. The Raman spectra were obtained during the hydrate formation at 30 or 60 min intervals, with an integration time of 1.0 s.

2.3.3. Powder X-ray Diffraction Analysis. The crystal structure of synthesized CO_2 hydrate in DW was determined by using PXRD, a widely accepted method for analyzing hydrate samples. First, a typical CO_2 hydrate formation experiment was performed with DW at 274.65 K and 3.5 MPa without Trp. Once hydrate formation was complete, the residual pressure inside the reactor was quickly vented, the reactor flange was removed, and the synthesized hydrates were instantly quenched with liquid nitrogen (∼77 K). Quenching allowed the sample collection of the hydrates, which were then crushed into a roughly uniform powder with a mortar and pestle in a liquid nitrogen environment. The liquid nitrogen helped to keep the synthesized hydrates stable while operating under atmospheric conditions. Finally, the hydrate powder was transferred to the in-house PXRD unit for characterization. The PXRD measurements were performed by using a BRUKER D8 advanced diffractometer (40 kV, 30 mA). The Cu Kα radiation (λ = 1.542 Å) was utilized as the X-ray. The PXRD patterns were collected in the 2θ range of 10−40°, with a 0.02° step size. Further details on the procedure used to calculate the lattice parameter of the synthesized hydrate crystals are given in the Supporting Information.[50]

2.4. Experimental Procedure. Before each experiment, the reactor was thoroughly cleaned and rinsed three times before adding water/DW. The reactor was then purged with CO_2 gas and vented three times to eliminate any remaining air. All experiments were conducted at a constant temperature within a closed system. The reactor was loaded with 40 g of pure water (density ∼1000 kg/m^3), 20 g of pure DW (density ∼500 kg/m^3), or 20 g of DW + 500/1000 ppm L-trp (density ∼500 kg/m^3).[32] Then, the system was allowed to cool to a temperature of 274.65 K. No agitation was employed in trials with pure water or DW. During the formation step, a pressure of 3.5 MPa was exerted on the system by introducing pure CO_2 gas into the reactor. The experimental conditions of 3.5 MPa and 274.65 K were selected to maximize the thermodynamic driving force for CO_2 hydrate formation, while ensuring that water in the DW system remained in the liquid state. The temperature of 274.65 K was chosen to prevent the freezing of water in DW, enabling clear observation of DW's kinetic promotion effects on hydrate formation with and without a kinetic promoter. Frozen water would obscure these effects. Upon pressurizing the system at a temperature of 274.65 K, CO_2 hydrate formation was detected by a sudden increase in system temperature and a subsequent pressure drop. The rise in temperature phenomenon can be attributed to hydrate formation releasing heat, which is an exothermic process. The front camera recorded the complete process of hydrate formation. To ensure the reproducibility of the results, each experiment was conducted at least twice. Trails with pure water are labeled A1 and A2; those with DW are labeled B1 and B2. Trails with DW + 500 ppm L-trp are labeled C1 and C2, and those with DW + 1000 ppm L-trp are labeled D1 and D2.

2.5. Calculation Procedure. The overall CO_2 uptake and the total amount of water transformed into CO_2 hydrate were estimated using the following equations.[4,51] Equation 1 was used to estimate the number of moles of CO_2 captured by CO_2 dissolving in the aqueous solution and solid hydrate phases at any given time.

$$\Delta n_t = \left[\frac{PV}{zRT}\right]_{t=0} - \left[\frac{PV}{zRT}\right]_t \text{ (mol)} \quad (1)$$

The P and T represent the pressure and temperature (recorded during the experiments), respectively; R is the universal gas constant, and t is any time during the experiment. Pitzer correlation[52] was used to calculate the compressibility factor z; P and T are measured at "0" (start of the experiment) and "t" (any time throughout the experiment) and V denotes the volume of the gas phase within the reactor.

By dividing the gas uptake from eq 1 by the moles of water in the system, one may determine the normalized gas uptake (mol of gas consumed per mole of water, mol/mol). Then, the normalized molar gas uptake (mol/mol) was converted into volumetric gas storage capacity (volume of gas (STP)/volume of hydrate) using the following equation[50]

$$\text{volumetric } CO_2 \text{ storage capacity}\left(\frac{\text{vol of gas (STP)}}{\text{vol of hydrate}}\right) = k\left(\frac{\Delta n_t}{n_w^o}\times 1000\right) \quad (2)$$

$$k = \frac{v}{M_{CO_2\text{hydrate}}/(\rho_{CO_2\text{hydrate}} \times 5.75)} \quad (3)$$

where the v,$M_{CO_2\text{hydrate}}$ and $\rho_{CO_2\text{hydrate}}$ stand for the volume of gas at STP (22.4 cm^3/mmol), the molar mass of CO_2 hydrate (1180 g) and density of CO_2 hydrate (1.1 g/cm^3).[26,53] Further, eq 4 was used to determine the fraction of water converted to gas hydrates.

$$\text{water conversion } (\%n_w^t) = \frac{5.75 \times \Delta n_t}{n_w^o} \times 100 \quad (4)$$

Here, n_w° (t = 0) is the total mole of water, and 5.75 is the hydration number derived from the literature.[46]

3. RESULTS AND DISCUSSION

3.1. Crystal Structure of DW-CO_2 Hydrate. Wang et al.[33] suggested that the reduced CO_2 uptake in DW-gas hydrates (∼150 v/v, compared to the theoretical capacity of sI hydrates, ∼180 v/v) could result from incomplete occupancy of the sI hydrate cages or the cocrystallization of sII with the sI phase. To the best of our knowledge, no studies have yet reported the structures of DW-CO_2 hydrates. Therefore, it is crucial to examine the crystal structure of DW-CO_2 hydrate using PXRD and in situ Raman spectroscopy (Figures 2 and 3).

For PXRD analysis, DW-CO_2 hydrate was prepared in the high-pressure reactor at initial conditions of 3.5 MPa and 274.65 K. Then, the hydrate sample was quenched and harvested at a liquid N_2 temperature (∼77 K). For data collection, the sample was prepared at ∼77 K to prevent hydrate dissociation under atmospheric pressure. Figure 2 presents the XRD pattern of pure hydrophobic nanosilica particles and the DW + CO_2 sample. The XRD pattern (black trace) depicted in Figure 2 exhibits a precise correspondence with the standard patterns of sI hydrates reported in the literature.[54,55] The calculated lattice parameter in the current study was 12.010 (±0.005) Å, closely matching the reported value of 12.070 Å.[56] This strong agreement provides compelling evidence that only sI hydrates were produced. Details of the calculation of the lattice parameter are given in the Supporting Information. During PXRD analysis, unreacted

https://doi.org/10.1021/acsami.4c17727
ACS Appl. Mater. Interfaces XXXX, XXX, XXX−XXX

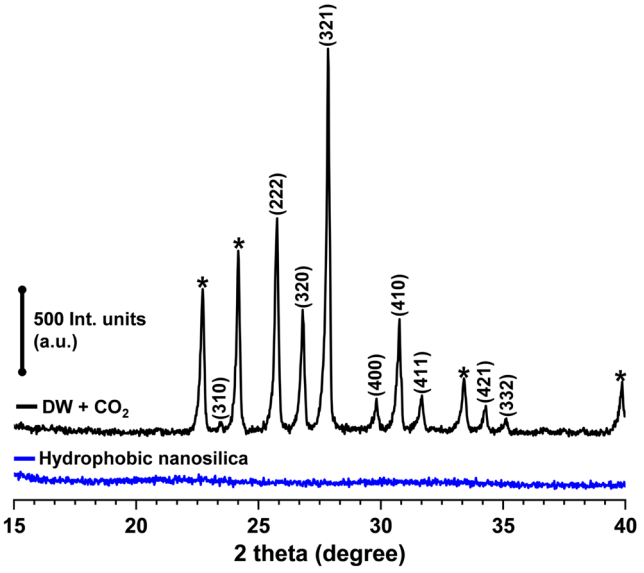

Figure 2. PXRD pattern of the DW + CO_2 sample (black trace) and of pure hydrophobic nanosilica particles (blue trace). After hydrate formation under initial conditions of 3.5 MPa and 274.65 K, DW-CO_2 hydrate was harvested at ~77 K for PXRD analysis. The peaks corresponding to the sI hydrate are marked by their corresponding (*hkl*) values, while the asterisks indicate the presence of ice Ih. Hydrophobic nanosilica was featureless in the 2θ range of 15−40°.

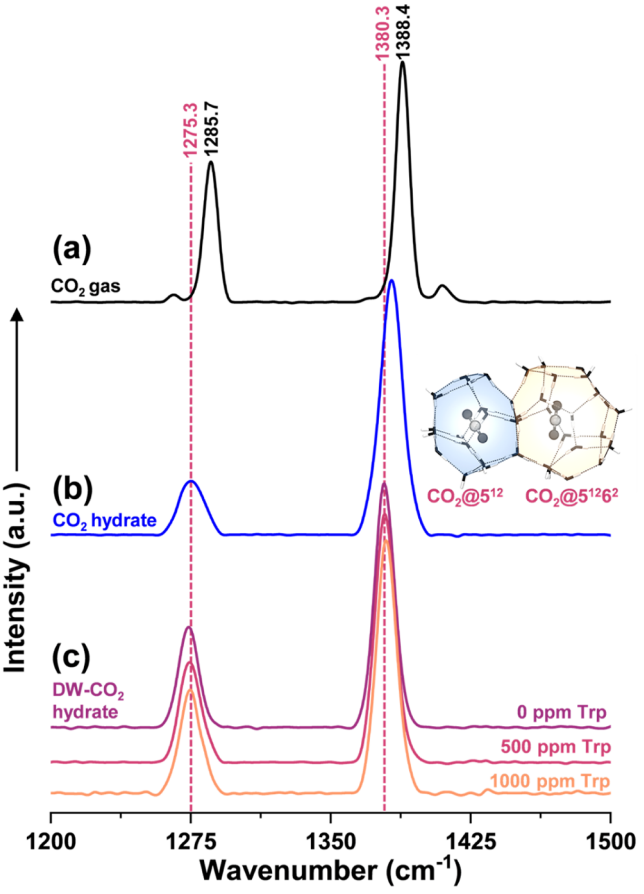

Figure 3. In situ Raman spectra of (a) CO_2 gas, (b) CO_2 hydrate prepared with pure water, and (c) CO_2 hydrate prepared with DW (0−1000 ppm L-trp). CO_2 hydrate, in all cases, was achieved at 3.5 MPa and 274.65 K.

water appeared as hexagonal ice, ice Ih (marked by asterisks), due to the sample being recovered at ~77 K (Figure 2). Moreover, hydrophobic nanosilica was featureless in the 2θ range of 15−40° (blue trace in Figure 2).

Further, using in situ Raman spectroscopy (a schematic diagram of the setup is shown in Figure S3), we independently analyzed the CO_2 hydrate formation in pure water and DW systems on a microscale under similar experimental conditions (3.5 MPa and 274.65 K). Figure 3 presents the Raman spectra for (a) pure CO_2 gas, (b) the CO_2 hydrate formed in pure water, and (c) the CO_2 hydrate formed in DW with and without Trp in the CO_2 Fermi dyad region. The obtained spectra for CO_2 hydrates formed in pure water and in DW (with or without L-trp) align perfectly with the Raman peaks of sI hydrates (Figure 3).[57,58] Time-dependent Raman spectra in the CO_2 Fermi dyad and the O−H stretching regions, showing the evolution of CO_2 hydrates, are detailed in Figure S4.

The identification of sI hydrates was determined by the presence of two Fermi dyad peaks at ~1380.3 and 1275.3 cm^{-1}, as established in the literature.[57−59] This confirms the formation of exclusively sI hydrates in the CO_2-DW systems under the experimental conditions of 3.5 MPa and 274.65 K. Thus, the current work provides the first-ever comprehensive in situ Raman and PXRD analysis for the formation of DW-CO_2 hydrate. So, the reduced CO_2 uptake in DW systems may primarily be due to incomplete occupancy of the hydrate cages, given that CO_2 forms only sI hydrates in these systems. The incomplete occupancies or reduced gas uptake may also be linked to the decreasing pH of the water content in DW, which results from the dissolution of CO_2 over time. However, this hypothesis must be confirmed by further research.

3.2. CO_2 Hydrate Growth Dynamics in DW. DW is a water-in-air dispersion primarily composed of water and stabilized by hydrophobic nanosilica particles (Figure 1). DW accelerates hydrate formation compared to bulk water by increasing the surface area for gas−water contact, which enhances gas dissolution and promotes the formation of hydrate nuclei and water-guest clusters.[32,60] According to Li et al.,[37] gas hydrate formation in DW involves two consecutive steps. Initially, the guest gas permeates a hydrophobic silica shell and enters the water core, and then the interaction between the guest gas and water molecules results in the formation of a gas hydrate.

However, there are conflicting reports about whether hydrate shells form on or beneath the silica shell (Figure 4).[35,48,61] To understand the hydrate growth dynamics in DW, Zhang et al.[61] used a modified shrinking core model by incorporating the effects of dissolved gas, capillary effects of the porous hydrate shell, and the volume change from water to hydrate. They found that the hydrate film initially forms on the outer surface of water droplets beneath the silica shell, where the gas concentration is the highest. Then, as gas diffuses through the hydrate shell, the hydrate grows inward at the hydrate−water interface. Additionally, due to water moving outward through capillaries (because of volume expansion upon hydrate formation), hydrates grow on the outer surface of the preformed hydrate shell (at the hydrate−gas interface) within the silica shell, causing the outer radius of DW to grow continuously (Figure 4a). Conversely, Park et al. utilized PXRD and Raman spectroscopy to conclude that the hydrate shell forms on the surface of DW above the silica shell.[35] They attributed this to the chemical potential difference between water molecules in hydrate cages and free water molecules in

https://doi.org/10.1021/acsami.4c17727
ACS Appl. Mater. Interfaces XXXX, XXX, XXX−XXX

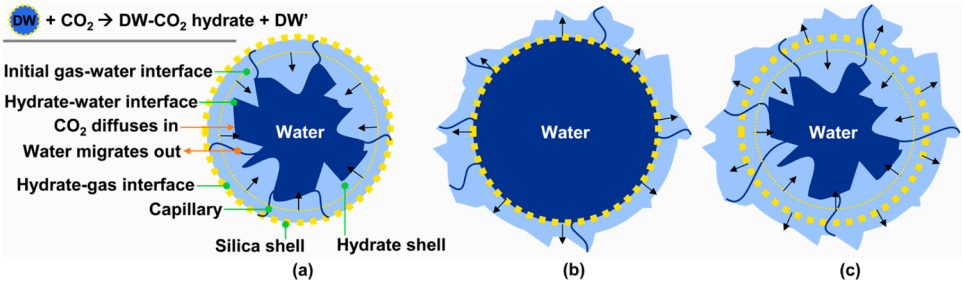

Figure 4. Physical model of the hydrate growth dynamics in DW systems. The top left corner displays the reaction scheme for the interaction between the guest gas and DW. Schematic (a) depicts the modified shrinking core model, indicating hydrate formation beneath the silica shell. Schematic (b) illustrates hydrate growth on the surface of DW particle. Schematic (c), based on PXRD and Raman analysis from the current work, demonstrates hydrate growth both on and beneath the silica shell. Key components of DW and DW-gas hydrates are labeled in (a). According to the shrinking core model, CO_2 diffuses through a porous hydrate shell in the water core and forms a hydrate at the hydrate−water interface, while water migrates out through capillaries and forms a hydrate at the hydrate−gas interface.

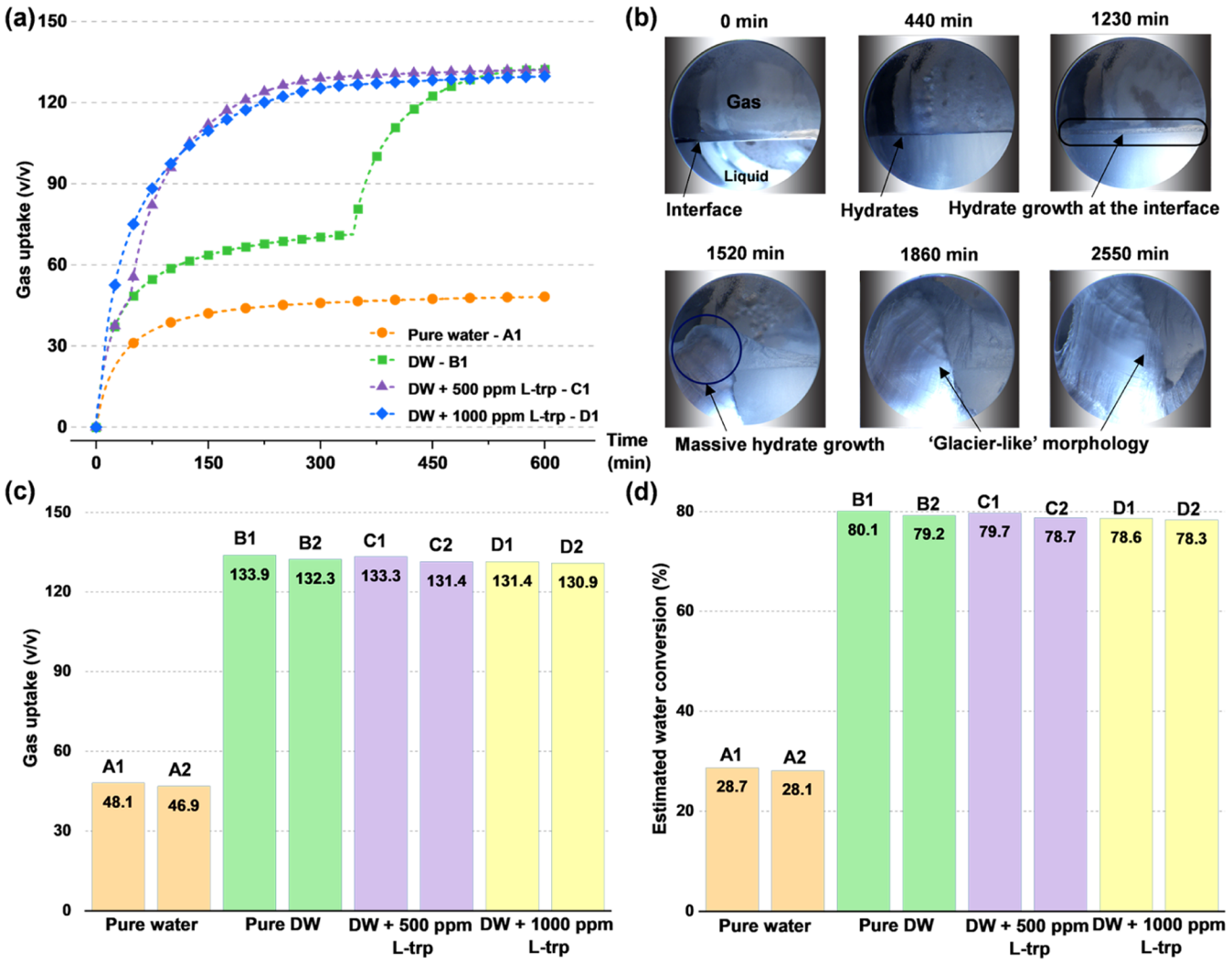

Figure 5. (a) Normalized CO_2 uptake achieved in trails A1 (pure water and orange trace), B1 (DW, green trace), C1 (DW + 500 ppm L-trp, violet trace), and D1 (DW + 1000 ppm L-trp, blue trace). CO_2 uptake in each case was estimated based on the experimentally observed changes in temperature and pressure, starting from initial conditions of 3.5 MPa and 274.65 K. Normalized gas uptake is depicted in volumetric gas storage capacity (volume of gas (STP)/volume of hydrate, v/v). (b) Morphology of CO_2 hydrate formation in pure water without L-trp and without mechanical agitation at 3.5 MPa and 274.65 K. Comparison of the (c) CO_2 uptakes and (d) water-to-hydrate conversions obtained for pure water (trails A1, and A2), DW (trails B1, and B2), DW + 500 ppm L-trp (trails C1, and C2), and DW + 1000 ppm L-trp (trails D1, and D2). In each experiment, the results from both trials were consistent, ensuring reliability.

DW particles, causing water to migrate out and form an external hydrate shell (Figure 4b). However, our current work reveals a different scenario. We found that the CO_2 hydrate in DW forms both on and beneath the silica shell. Unlike Park et

https://doi.org/10.1021/acsami.4c17727
ACS Appl. Mater. Interfaces XXXX, XXX, XXX−XXX

Table 1. Estimated Water Conversion, Gas Uptake, Induction Time, and t_{90}, for Each Trial

system	trails	estimated water conversion (%)	estimated gas uptake (volume of gas at STP/volume of hydrate)	induction time (min)	t_{90} (min)
pure water	A1	28.7	48.1	212.5	164.3
	A2	28.1	46.9	714.3	295.3
DW + 0 ppm L-trp	B1	80.1	133.9	64.2	439.2
	B2	79.2	132.3	85.4	1085.2
DW + 500 ppm L-trp	C1	79.7	133.3	48.8	192.7
	C2	78.7	131.4	52.5	175.7
DW + 1000 ppm L-trp	D1	78.6	131.4	7.8	209.7
	D2	78.3	130.9	4.3	192.7

al., who did not observe a broad signal from silica particles in the 2θ range of 10−15° in their PXRD analysis—interpreting this as evidence of a hydrate shell covering DW particles. We observed a broad signal in our PXRD pattern (Figure S5a), indicating hydrate formation within the silica shell of DW. Additionally, the reduction in peak intensity of the Si−O−Si stretching band in Raman spectra (Figure S5b) suggests that a small fraction of the hydrates was also formed above the silica shell (Figure 4c). However, Park et al. noted a complete disappearance of the Si−O−Si stretching band in the Raman spectra after hydrate formation. This PXRD and Raman analysis confirms our findings and provides a nuanced understanding of hydrate formation in the CO_2-DW systems. All three scenarios of hydrate growth dynamics in DW are depicted in Figure 4(a−c).

Previously, DW-gas hydrates have been tested for reusability through multiple hydrate formation-dissociation cycles.[33,35] Notably, the hydrate shells that form on DW will convert to free water upon dissociation and will not re-enter DW without high-speed reblending. Park et al.[35] observed that in the first formation-dissociation cycle, approximately 80% of the water was converted to hydrate covering the silica shell, meaning this 80% will become free water after dissociation. This indicates that only about 20% of the water remains inside the DW for the second cycle. However, in their second cycle with the same sample, they found that around 50% of the water converted to hydrate, which cannot be explained by the hypothesis that hydrate shells form solely above the silica shells. Our hypothesis provides a more comprehensive explanation: hydrates can grow on and beneath the silica shell, and only the fraction of hydrates formed above the silica shell converts to free water, while the remaining water stays inside DW. This means that during hydrate dissociation, while the hydrate formed above the silica shell accounts for the free water, the hydrate formed beneath the silica shell retains water within the silica shell, ensuring the stability and reusability of DW. This dual hydrate growth dynamics—hydrates forming both on and beneath the silica shell—explains the observed reusability and water retention in DW, offering a better understanding of the hydrate formation-dissociation processes.

3.3. Formation Kinetics and Morphology of CO_2 Hydrates in Pure Water, DW, and DW + L-trp.

Understanding the kinetic characteristics of hydrate formation is crucial for evaluating the potential of hydrate-based carbon capture and storage (HBCS) technology. This study investigates the CO_2 hydrate formation kinetics and morphology in three systems: pure water, DW, and DW with 500 and 1000 ppm of L-trp. Here, L-trp is used as a kinetic hydrate promoter. All experiments were conducted with an initial temperature of 274.65 K and a pressure of 3.5 MPa, and each was repeated twice to ensure reliable results. From the recorded temperature and pressure data, we estimated the CO_2 uptake, water-to-hydrate conversion, induction time, and time required to reach 90% gas uptake (t_{90}) for all systems, providing a comprehensive comparison of their kinetic performance. To establish a baseline for CO_2 hydrate formation kinetics, initial experiments were conducted using pure water. Changes in the pressure and temperature during the hydrate formation process are shown in Figure S6a. The CO_2 gas uptake kinetics for pure water are presented in Figure 5a (orange trace), while the morphology of hydrate formation is illustrated in Figure 5b. In two experimental trials with pure water, normalized gas uptake was 48.1 v/v with a 28.75% water-to-hydrate conversion in trial A1 and 46.9 v/v with a 28.11% conversion in trial A2 (Figure 5c,d). Induction time and t_{90} are detailed in Table 1.

Figure 5b reveals the morphology of the CO_2 hydrate formed in pure water. We observed that initially, as CO_2 dissolves, the solution turns from translucent to milky white. After ∼420 min, a thin hydrate film forms at the gas−water interface and grows slowly until ∼1200 min. At this stage, a branch-like crystal emerges from the reactor's edge, causing the thin film to rupture due to volume expansion. This rupture triggers spontaneous, rapid hydrate formation throughout the reactor aided by enhanced CO_2 diffusion. By 1800 min, bulk hydrates with a "glacier-like appearance" are visible (Figure 5b and Video S1). This overall process occurs in three stages: nucleation, film formation, and film breakup with bulk hydrate growth.[13,53] While, Dhamu et al.[13] reported different types of CO_2 hydrate morphologies, which included fine caladium-like crystalline growth, hydrate dendrites, hydrate glaciers, and atrichous-hydrate branchlets. In the present case, we observed an atrichous-hydrate branchlet at ∼1500 min and a glacier-like morphology at ∼1800 min.[27]

The next set of experiments was conducted by using DW and DW + L-trp. The changes in pressure and temperature during CO_2 hydrate formation in these systems are shown in Figure S6b−d. Figure 5a,c,d presents the CO_2 gas uptakes and water conversions achieved with DW + (0−1000 ppm) L-trp. The CO_2 uptake in DW was estimated to be 133.9 v/v with a water-to-hydrate conversion of 80.1% for trail B1 and 132.3 v/v with a water-to-hydrate conversion of 79.2% for trail B2 (Figure 5c,d). Hence, the CO_2 gas uptake in DW was about ∼2.8 times higher than that of pure water (∼48 v/v).

To optimize the DW-CO_2 hydrate formation kinetics above the freezing point, L-trp was used as a kinetic promoter in DW. L-trp concentrations of 500 and 1000 ppm were tested, and DW prepared with L-trp-doped solutions remained stable for over 1 month. The CO_2 uptake and water-to-hydrate conversion in DW with 500 ppm L-trp (C1 and C2) and

https://doi.org/10.1021/acsami.4c17727
ACS Appl. Mater. Interfaces XXXX, XXX, XXX−XXX

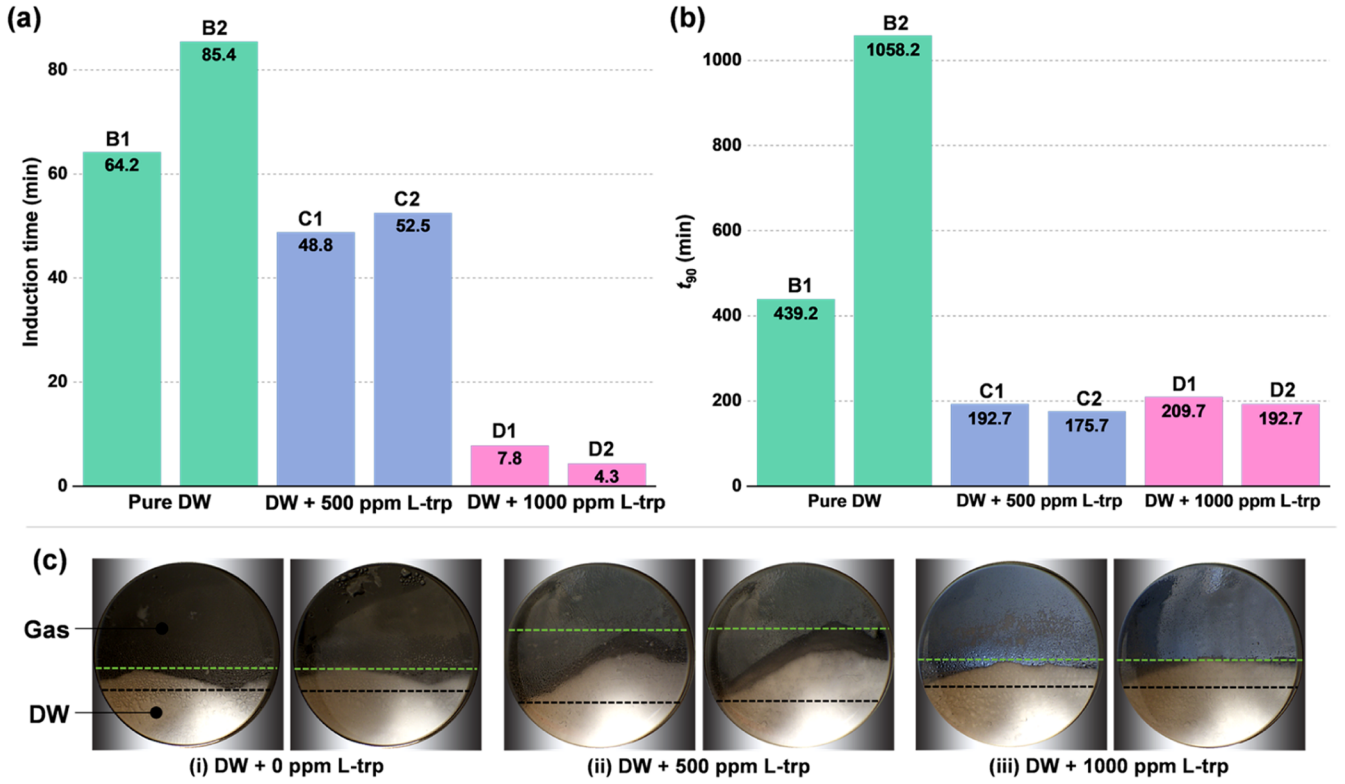

Figure 6. Comparison of the (a) induction time, and (b) the time required to reach 90% completion of gas uptake (t_{90}) for DW (trails B1, and B2), DW + 500 ppm L-trp (trails C1, and C2), and DW + 1000 ppm L-trp (trails D1, and D2). (C) Comparison of the DW-CO_2 hydrate morphology before (initial) and after (final) the hydrate formation in (i) DW, (ii) DW + 500 ppm L-trp, and (iii) DW + 1000 ppm L-trp systems at 3.5 MPa and 274.65 K. Changes in DW can be visualized between the black and green dotted lines, drawn at the lowest and highest heights of the initial morphology, respectively. During hydrate formation, an increase in the height of the DW column was observed with a simultaneous change in the temperature and pressure. During pressurization, the initial arrangements of DW change, unlike in liquid water.

1000 ppm L-trp (D1 and D2) were comparable to those observed in pure DW, as presented in Table 1 and Figure 5c,d. This demonstrates that both L-trp-doped and pure DW exhibit high CO_2 uptake and rapid hydrate formation compared with pure water. Further, Figure 6a,6b present the induction time and t_{90} for CO_2 hydrate formation in DW with and without L-trp. We observed that the addition of L-trp leads to a roughly linear decrease in induction time with increasing L-trp concentration (Figure 6a). Although L-trp doping in DW significantly reduces t_{90}, the values for 500 and 1000 ppm of L-trp are similar (Figure 6b). Furthermore, the nucleation and growth of CO_2 hydrates in pure DW at 274.65 K exhibited stochastic behavior (Figure 6a,b), meaning that the process was less predictable and highly variable, similar to hydrate formation in pure water. While the variability is not fully understood, incorporating additives like L-trp (as observed in this study) or lowering the formation temperature[33] can reduce this stochastic behavior. Future studies will focus on understanding the behavior of pure DW at higher temperatures. Table 1 summarizes the CO_2 uptake, water-to-hydrate conversion, induction time, and t_{90} values for each experimental trial.

The morphology of the CO_2 hydrate formation in DW + (0−1000 ppm) L-trp is shown in Figure 6c. The initial arrangement of the DW particles inside the high-pressure reactor changes slightly during the CO_2 pressurization, as evidenced by the column heights for different trials shown in Figure 6c. During the formation of the CO_2 hydrate in DW, detected by a simultaneous rise in temperature and drop in pressure, a slight change in DW arrangement or increase in the height of the DW column was observed (Figure 6c, Videos S2, S3, and S4). The change in the DW arrangement before and after hydrate formation can be realized by seeing between black and green dotted lines in Figure 6c. However, compared to pure water, the morphological growth pattern of CO_2 hydrates in DW is difficult to observe as both DW-CO_2 hydrate and DW have a similar white appearance.

From the foregoing, we understand that DW offers clear advantages for CO_2 storage in hydrates by eliminating the need for mechanical stirring or additional promoters. Our findings indicate that incorporating L-trp into DW significantly accelerates hydrate formation, reducing both induction time and t_{90} at 274.65 K. L-trp, well-established for its kinetic promotion of CO_2/CH_4 hydrate formation in liquid water, operates through its amphiphilic structure, which (i) lowers interfacial tension, (ii) facilitates gas transfer, and (iii) arranges water molecules to accelerate nucleation and stabilize hydrate structures.[41] Since the current set of DW experiments were conducted above freezing point (274.65 K, water inside silica shell will remain in liquid phase), we anticipate similar promotion effects of L-trp in DW as observed in liquid water systems. Previous studies, like the one by Khandelwal et al.,[43] reported a maximum CO_2 uptake of approximately 116 v/v in water doped with L-trp. In contrast, our study demonstrates that pure DW achieves a CO_2 uptake of about 134 v/v. This distinction is critical for assessing the commercial potential of DW in CO_2 storage applications. Our future research will focus on screening new thermodynamic promoters for enhancing

https://doi.org/10.1021/acsami.4c17727
ACS Appl. Mater. Interfaces XXXX, XXX, XXX−XXX

DW stability to improve hydrate formation kinetics further at lower pressures and ambient temperatures.

4. CONCLUSIONS

We conducted a detailed experimental investigation into the formation of CO_2 hydrates in both pure water and DW doped with L-trp (0−1000 ppm) under conditions of 3.5 MPa and 274.65 K, without mechanical agitation. Through a comprehensive analysis employing a high-pressure reactor, PXRD, and in situ Raman spectroscopy, we explored critical aspects of DW-CO_2 hydrate, including crystal structure, hydrate growth dynamics, morphology, and gas uptake kinetics. The PXRD and Raman spectroscopy data unequivocally confirm the formation of sI hydrate in DW, revealing the incomplete occupancy of hydrate cages, which could be one of the reasons for the reduction in CO_2 uptake in DW systems. Our findings notably demonstrate the existence of hydrate shells both on and beneath the silica shell. This insight into hydrate growth dynamics is crucial for understanding the reusability of DW. Moreover, kinetic studies demonstrated that the CO_2 gas uptake in DW is approximately three times higher than in pure water, highlighting the suitability of DW for CCS. Our findings also indicate that doping DW with L-trp does not significantly enhance CO_2 uptake, though it effectively reduces stochasticity, induction time and t_{90}. These characteristics emphasize DW's potential as an energy-efficient and suitable solution for CO_2 storage, with significant implications for large-scale deployment.

■ ASSOCIATED CONTENT

Supporting Information

The Supporting Information is available free of charge at https://pubs.acs.org/doi/10.1021/acsami.4c17727.

Additional experimental details, schematics of experimental setups, Raman spectra, and P-T plots (PDF)

CO_2 hydrate formation morphology in pure water (Video S1) (MP4)

CO_2 hydrate formation morphology in dry water (Video S2) (MP4)

CO_2 hydrate formation morphology in dry water +500 ppm L-trp (Video S3) (MP4)

CO_2 hydrate formation morphology in dry water +1000 ppm L-trp (Video S4) (MP4)

■ AUTHOR INFORMATION

Corresponding Authors

Thalappil Pradeep − *DST Unit of Nanoscience (DST UNS) and Thematic Unit of Excellence (TUE), Department of Chemistry, Indian Institute of Technology Madras, Chennai 600036, India; International Centre for Clean Water, IIT Madras Research Park, Chennai 600113, India;* orcid.org/0000-0003-3174-534X; Email: pradeep@iitm.ac.in

Praveen Linga − *Department of Chemical and Biomolecular Engineering, National University of Singapore, Singapore 117580, Singapore;* orcid.org/0000-0002-1466-038X; Email: praveen.linga@nus.edu.sg

Authors

Gaurav Vishwakarma − *Department of Chemical and Biomolecular Engineering, National University of Singapore, Singapore 117580, Singapore; DST Unit of Nanoscience (DST UNS) and Thematic Unit of Excellence (TUE), Department of Chemistry, Indian Institute of Technology Madras, Chennai 600036, India;* orcid.org/0009-0002-6076-3299

Vikas Dhamu − *Department of Chemical and Biomolecular Engineering, National University of Singapore, Singapore 117580, Singapore*

M. Fahed Qureshi − *Department of Chemical and Biomolecular Engineering, National University of Singapore, Singapore 117580, Singapore*

Gaurav Bhattacharjee − *Department of Chemical and Biomolecular Engineering, National University of Singapore, Singapore 117580, Singapore;* orcid.org/0000-0001-5284-2785

Complete contact information is available at: https://pubs.acs.org/10.1021/acsami.4c17727

Author Contributions

‖G.V. and V.D. contributed equally to this work. P.L. and T.P. supervised the project. P.L., T.P., G.V., V.D., M.F.Q., and G. B. conceptualized the work and designed the experiments. G.V. and V.D. carried out the experiments and data analytics. All authors contributed to writing the manuscript, reviewed the final draft, and approved its submission.

Notes

The authors declare no competing financial interest.

■ ACKNOWLEDGMENTS

P.L. acknowledges the funding support from the Agency of Science, Technology and Research (A*STAR) under the Low-Carbon Energy Research (LCER) Funding Initiatives (Project U2102d2010). T.P. acknowledges funding from the Centre of Excellence on Molecular Materials and Functions under the Institution of Eminence scheme of IIT Madras. G.V. thanks IIT Madras for providing the research fellowship and the International Immersion Experience (IIE) travel grant.

■ REFERENCES

(1) Meinshausen, M.; Jeffery, L.; Guetschow, J.; Robiou du Pont, Y.; Rogelj, J.; Schaeffer, M.; Höhne, N.; den Elzen, M.; Oberthür, S.; Meinshausen, N. National post-2020 greenhouse gas targets and diversity-aware leadership. *Nat. Clim. Change* **2015**, *5* (12), 1098−1106.

(2) Staniaszek, Z.; Griffiths, P. T.; Folberth, G. A.; O'Connor, F. M.; Abraham, N. L.; Archibald, A. T. The role of future anthropogenic methane emissions in air quality and climate. *npj Clim. Atmos. Sci.* **2022**, *5* (1), No. 21.

(3) Qureshi, M. F.; Zheng, J.; Khandelwal, H.; Venkataraman, P.; Usadi, A.; Barckholtz, T. A.; Mhadeshwar, A. B.; Linga, P. Laboratory demonstration of the stability of CO2 hydrates in deep-oceanic sediments. *Chem. Eng. J.* **2022**, *432*, No. 134290.

(4) Qureshi, M. F.; Khandelwal, H.; Usadi, A.; Barckholtz, T. A.; Mhadeshwar, A. B.; Linga, P. CO2 hydrate stability in oceanic sediments under brine conditions. *Energy* **2022**, *256*, No. 124625.

(5) Lee, H.; Lee, J.-w.; Kim, D. Y.; Park, J.; Seo, Y.-T.; Zeng, H.; Moudrakovski, I. L.; Ratcliffe, C. I.; Ripmeester, J. A. Tuning clathrate hydrates for hydrogen storage. *Nature* **2005**, *434* (7034), 743−746.

(6) Zheng, J.; Chong, Z. R.; Qureshi, M. F.; Linga, P. Carbon Dioxide Sequestration via Gas Hydrates: A Potential Pathway toward Decarbonization. *Energy Fuels* **2020**, *34* (9), 10529−10546.

(7) Sloan, E. D. Fundamental principles and applications of natural gas hydrates. *Nature* **2003**, *426* (6964), 353−359.

(8) Berni, S.; Scelta, D.; Romi, S.; Fanetti, S.; Alabarse, F.; Pagliai, M.; Bini, R. Exploring High-Pressure Polymorphism in Carbonic Acid

through Direct Synthesis from Carbon Dioxide Clathrate Hydrate. *Angew. Chem., Int. Ed.* **2024**, No. e202403953.
(9) Ghosh, J.; Vishwakarma, G.; Kumar, R.; Pradeep, T. Formation and Transformation of Clathrate Hydrates under Interstellar Conditions. *Acc. Chem. Res.* **2023**, *56* (16), 2241−2252.
(10) Vishwakarma, G.; Malla, B. K.; Reddy, K. S. S. V. P.; Ghosh, J.; Chowdhury, S.; Yamijala, S. S. R. K. C.; Reddy, S. K.; Kumar, R.; Pradeep, T. Induced Migration of CO2 from Hydrate Cages to Amorphous Solid Water under Ultrahigh Vacuum and Cryogenic Conditions. *J. Phys. Chem. Lett.* **2023**, *14* (11), 2823−2829.
(11) Vishwakarma, G.; Malla, B. K.; Kumar, R.; Pradeep, T. Partitioning photochemically formed CO2 into clathrate hydrate under interstellar conditions. *Phys. Chem. Chem. Phys.* **2024**, *26* (22), 16008−16016.
(12) Dhamu, V.; Mengqi, X.; Qureshi, M. F.; Yin, Z.; Jana, A. K.; Linga, P. Evaluating CO2 hydrate kinetics in multi-layered sediments using experimental and machine learning approach: Applicable to CO2 sequestration. *Energy* **2024**, *290*, No. 129947.
(13) Dhamu, V.; Qureshi, M. F.; Abubakar, S.; Usadi, A.; Barckholtz, T. A.; Mhadeshwar, A. B.; Linga, P. Investigating High-Pressure Liquid CO2 Hydrate Formation, Dissociation Kinetics, and Morphology in Brine and Freshwater Static Systems. *Energy Fuels* **2023**, *37* (12), 8406−8420.
(14) Ren, M.; Sevilla, M.; Fuertes, A. B.; Mokaya, R.; Tour, J. M.; Jalilov, A. S. Pore Characteristics for Efficient CO2 Storage in Hydrated Carbons. *ACS Appl. Mater. Interfaces* **2019**, *11* (47), 44390−44398.
(15) Cao, P.; Ning, F.; Wu, J.; Cao, B.; Li, T.; Sveinsson, H. A.; Liu, Z.; Vlugt, T. J. H.; Hyodo, M. Mechanical Response of Nanocrystalline Ice-Contained Methane Hydrates: Key Role of Water Ice. *ACS Appl. Mater. Interfaces* **2020**, *12* (12), 14016−14028.
(16) Cao, P.; Li, T.; Ning, F.; Wu, J. Mechanical Instability of Methane Hydrate−Mineral Interface Systems. *ACS Appl. Mater. Interfaces* **2021**, *13* (38), 46043−46054.
(17) Phan, A.; Stamatakis, M.; Koh, C. A.; Striolo, A. Correlating Antiagglomerant Performance with Gas Hydrate Cohesion. *ACS Appl. Mater. Interfaces* **2021**, *13* (33), 40002−40012.
(18) Kim, B.; Zhang, Y. G. Methane hydrate dissociation across the Oligocene−Miocene boundary. *Nat. Geosci.* **2022**, *15* (3), 203−209.
(19) Liang, M.; Chen, G.; Sun, C.; Yan, L.; Liu, J.; Ma, Q. Experimental and modeling study on decomposition kinetics of methane hydrates in different media. *J. Phys. Chem. B* **2005**, *109* (40), 19034−19041.
(20) Ghosh, J.; Bhuin, R. G.; Vishwakarma, G.; Pradeep, T. Formation of Cubic Ice via Clathrate Hydrate, Prepared in Ultrahigh Vacuum under Cryogenic Conditions. *J. Phys. Chem. Lett.* **2020**, *11* (1), 26−32.
(21) Ghosh, J.; Vishwakarma, G.; Das, S.; Pradeep, T. Facile Crystallization of Ice Ih via Formaldehyde Hydrate in Ultrahigh Vacuum under Cryogenic Conditions. *J. Phys. Chem. C* **2021**, *125* (8), 4532−4539.
(22) Vishwakarma, G.; Malla, B. K.; Chowdhury, S.; Khandare, S. P.; Pradeep, T. Existence of Acetaldehyde Clathrate Hydrate and Its Dissociation Leading to Cubic Ice under Ultrahigh Vacuum and Cryogenic Conditions. *J. Phys. Chem. Lett.* **2023**, *14* (23), 5328−5334.
(23) Aminnaji, M.; Qureshi, M. F.; Dashti, H.; Hase, A.; Mosalanejad, A.; Jahanbakhsh, A.; Babaei, M.; Amiri, A.; Maroto-Valer, M. CO2 gas hydrate for carbon capture and storage applications − Part 2. *Energy* **2024**, *300*, No. 131580.
(24) Aminnaji, M.; Qureshi, M. F.; Dashti, H.; Hase, A.; Mosalanejad, A.; Jahanbakhsh, A.; Babaei, M.; Amiri, A.; Maroto-Valer, M. CO2 Gas hydrate for carbon capture and storage applications − Part 1. *Energy* **2024**, *300*, No. 131579.
(25) Davies, R. J.; Yang, J.; Ireland, M. T.; Berndt, C.; Maqueda, M. Á. M.; Huuse, M. Long-distance migration and venting of methane from the base of the hydrate stability zone. *Nat. Geosci.* **2024**, *17* (1), 32−37.
(26) Dhamu, V.; Qureshi, M. F.; Barckholtz, T. A.; Mhadeshwar, A. B.; Linga, P. Evaluating liquid CO2 hydrate formation kinetics, morphology, and stability in oceanic sediments on a lab scale using top injection. *Chem. Eng. J.* **2023**, *478*, No. 147200.
(27) Dhamu, V.; Xiao, M.; Qureshi, M. F.; Linga, P. Deciphering the CO2 hydrates formation dynamics in brine-saturated oceanic sediments using experimental and machine learning modelling approach. *Energy* **2024**, *313*, No. 133802.
(28) Veluswamy, H. P. Energy Storage in Hydrates: Status, Recent Trends, and Future Prospects. *ACS Appl. Energy Mater.* **2024**, *7*, 11497−11515.
(29) Burla, S. K.; Pagar, E.; Veluswamy, H. P. Synergistic CH4 Recovery and CO2 Sequestration through Amino Acid-Assisted Injection in Methane Hydrate Sediments. *Energy* **2024**, *304*, No. 132089.
(30) Alhejaili, A.; Babu, P.; Daraboina, N. Impact of chloride salts on TBAB/Methane and TBAB/Carbon dioxide semiclathrate hydrates: Application to desalination. *Fluid Phase Equilib.* **2024**, *583*, No. 114128.
(31) Babu, P.; Alhejaili, A.; Bollineni, C.; Daraboina, N. Phase Equilibrium of Carbon Dioxide/Tetra-n-butyl Ammonium Bromide Mixed Hydrate in the Presence of Produced Water. *J. Chem. Eng. Data* **2024**, *69* (3), 1307−1313.
(32) Wang, W.; Bray, C. L.; Adams, D. J.; Cooper, A. I. Methane Storage in Dry Water Gas Hydrates. *J. Am. Chem. Soc.* **2008**, *130* (35), 11608−11609.
(33) Carter, B. O.; Wang, W.; Adams, D. J.; Cooper, A. I. Gas Storage in "Dry Water" and "Dry Gel" Clathrates. *Langmuir* **2010**, *26* (5), 3186−3193.
(34) Binks, B. P.; Murakami, R. Phase inversion of particle-stabilized materials from foams to dry water. *Nat. Mater.* **2006**, *5* (11), 865−869.
(35) Park, J.; Shin, K.; Kim, J.; Lee, H.; Seo, Y.; Maeda, N.; Tian, W.; Wood, C. D. Effect of hydrate shell formation on the stability of dry water. *J. Phys. Chem. C* **2015**, *119* (4), 1690−1699.
(36) Hu, G.; Ye, Y.; Liu, C.; Meng, Q.; Zhang, J.; Diao, S. Direct measurement of formation and dissociation rate and storage capacity of dry water methane hydrates. *Fuel Process. Technol.* **2011**, *92* (8), 1617−1622.
(37) Li, Y.; Zhang, D.; Bai, D.; Li, S.; Wang, X.; Zhou, W. Size Effect of Silica Shell on Gas Uptake Kinetics in Dry Water. *Langmuir* **2016**, *32* (29), 7365−7371.
(38) Podenko, L. S.; Drachuk, A. O.; Molokitina, N. S.; Nesterov, A. N. Effect of Silica Nanoparticles on Dry Water Gas Hydrate Formation and Self-Preservation Efficiency. *Russ. J. Phys. Chem. A* **2018**, *92* (2), 255−261.
(39) Podenko, L. S.; Nesterov, A. N.; Drachuk, A. O.; Molokitina, N. S.; Reshetnikov, A. M. Formation of propane hydrates in Frozed dry water. *Russ. J. Appl. Chem.* **2013**, *86* (10), 1509−1514.
(40) Golkhou, F.; Haghtalab, A. Kinetic and thermodynamic study of CO2 storage in reversible gellan gum supported dry water clathrates. *J. Taiwan Inst. Chem. Eng.* **2020**, *115*, 79−95.
(41) Bhattacharjee, G.; Linga, P. Amino Acids as Kinetic Promoters for Gas Hydrate Applications: A Mini Review. *Energy Fuels* **2021**, *35* (9), 7553−7571.
(42) Qureshi, M. F.; Khraisheh, M.; AlMomani, F. Probing the effect of various water fractions on methane (CH4) hydrate phase equilibria and hydrate inhibition performance of amino acid L-proline. *J. Mol. Liq.* **2021**, *333*, No. 115888.
(43) Khandelwal, H.; Qureshi, M. F.; Zheng, J.; Venkataraman, P.; Barckholtz, T. A.; Mhadeshwar, A. B.; Linga, P. Effect of l-Tryptophan in Promoting the Kinetics of Carbon Dioxide Hydrate Formation. *Energy Fuels* **2021**, *35* (1), 649−658.
(44) Jeenmuang, K.; Pornaroontham, P.; Qureshi, M. F.; Linga, P.; Rangsunvigit, P. Micro kinetic analysis of the CO2 hydrate formation and dissociation with L-tryptophan in brine via high pressure in situ Raman spectroscopy for CO2 sequestration. *Chem. Eng. J.* **2024**, *479*, No. 147691.
(45) Zebardast, S.; Haghtalab, A. Thermodynamic modeling and measurement of CO2 clathrate equilibrium conditions with a

https://doi.org/10.1021/acsami.4c17727
ACS Appl. Mater. Interfaces XXXX, XXX, XXX−XXX

hydrophobic surface − An application in dry water hydrate. *Chem. Eng. Sci.* **2022**, *251*, No. 117486.
(46) Wei, Y.; Maeda, N. Kinetic promotion of gas hydrate formations using dispersions. *Chem. Eng. Sci.* **2024**, *286*, No. 119673.
(47) Farhang, F.; Nguyen, A. V.; Sewell, K. B. Fundamental Investigation of the Effects of Hydrophobic Fumed Silica on the Formation of Carbon Dioxide Gas Hydrates. *Energy Fuels* **2014**, *28* (11), 7025−7037.
(48) Shi, B.-H.; Fan, S.-S.; Lou, X. Application of the shrinking-core model to the kinetics of repeated formation of methane hydrates in a system of mixed dry-water and porous hydrogel particulates. *Chem. Eng. Sci.* **2014**, *109*, 315−325.
(49) Altamash, T.; Khraisheh, M.; Qureshi, M. F. Investigating the effects of mixing ionic liquids on their density, decomposition temperature, and gas absorption. *Chem. Eng. Res. Des.* **2019**, *148*, 251−259.
(50) Bhattacharjee, G.; Goh, M. N.; Arumuganainar, S. E.; Zhang, Y.; Linga, P. Ultra-rapid uptake and the highly stable storage of methane as combustible ice. *Energy Environ. Sci.* **2020**, *13* (12), 4946−4961.
(51) Dhamu, V.; Thakre, N.; Jana, A. K. Structure-H hydrate of mixed gases: Phase equilibrium modeling and experimental validation. *J. Mol. Liq.* **2021**, *343*, No. 117605.
(52) Zheng, J.; Zhang, B.-Y.; Wu, Q.; Linga, P. Kinetic Evaluation of Cyclopentane as a Promoter for CO2 Capture via a Clathrate Process Employing Different Contact Modes. *ACS Sustainable Chem. Eng.* **2018**, *6* (9), 11913−11921.
(53) Dhamu, V.; Qureshi, M. F.; Selvaraj, N.; Yuanmin, L. J.; Guo, I. T.; Linga, P. Dual Promotional Effect of l-Tryptophan and 1,3-Dioxane on CO2 Hydrate Kinetics in Seawater under Static/Unstatic Conditions for Carbon Capture and Storage Application. *Energy Fuels* **2024**, *38*, 11980−11993.
(54) Kumar, A.; Daraboina, N.; Linga, P.; Kumar, R.; Ripmeester, J. A. Experimental study on hydrate structure transition using an in situ high-pressure powder X-ray diffractometer: application in CO2 capture. *ACS Sustainable Chem. Eng.* **2022**, *10* (35), 11473−11482.
(55) Jin, Y.; Kida, M.; Nagao, J. Clathrate Hydrates Coexisting Thiazole: Two Roles of Structure II Hydrate Former and Structure I Thermodynamic Inhibitor. *Energy Fuels* **2023**, *37* (3), 2467−2474.
(56) Koh, C. A.; Savidge, J. L.; Tang, C. C. Time-Resolved in-Situ Experiments on the Crystallization of Natural Gas Hydrates. *J. Phys. Chem. A* **1996**, *100* (16), 6412−6414.
(57) Qin, J.; Kuhs, W. F. Quantitative analysis of gas hydrates using Raman spectroscopy. *AlChE J.* **2013**, *59* (6), 2155−2167.
(58) Chen, L.; Lu, H.; Ripmeester, J. A. Raman spectroscopic study of CO2 in hydrate cages. *Chem. Eng. Sci.* **2015**, *138*, 706−711.
(59) Li, Y.; Gambelli, A. M.; Rossi, F.; Mei, S. Effect of promoters on CO2 hydrate formation: Thermodynamic assessment and microscale Raman spectroscopy/hydrate crystal morphology characterization analysis. *Fluid Phase Equilib.* **2021**, *550*, No. 113218.
(60) Forny, L.; Pezron, I.; Saleh, K.; Guigon, P.; Komunjer, L. Storing water in powder form by self-assembling hydrophobic silica nanoparticles. *Powder Technol.* **2007**, *171* (1), 15−24.
(61) Zhang, F.; Wang, X.; Wang, B.; Lou, X.; Lipiński, W. Experimental and numerical analysis of CO2 and CH4 hydrate formation kinetics in microparticles: A comparative study based on shrinking core model. *Chem. Eng. J.* **2022**, *446*, No. 137247.

https://doi.org/10.1021/acsami.4c17727
ACS Appl. Mater. Interfaces XXXX, XXX, XXX−XXX